

A flatter gallium profile for high-efficiency Cu(In,Ga)(Se,S)₂ solar cell and improved robustness against sulfur-gradient variation

Chien-Yao Huang, Wen-Chin Lee, and Albert Lin

Citation: [Journal of Applied Physics](#) **120**, 094502 (2016); doi: 10.1063/1.4961605

View online: <http://dx.doi.org/10.1063/1.4961605>

View Table of Contents: <http://scitation.aip.org/content/aip/journal/jap/120/9?ver=pdfcov>

Published by the [AIP Publishing](#)

Articles you may be interested in

[New insights into the Mo/Cu\(In,Ga\)Se₂ interface in thin film solar cells: Formation and properties of the MoSe₂ interfacial layer](#)

[J. Chem. Phys.](#) **145**, 154702 (2016); 10.1063/1.4964677

[Reliable wet-chemical cleaning of natively oxidized high-efficiency Cu\(In,Ga\)Se₂ thin-film solar cell absorbers](#)

[J. Appl. Phys.](#) **116**, 233502 (2014); 10.1063/1.4903976

[Intergrain variations of the chemical and electronic surface structure of polycrystalline Cu\(In,Ga\)Se₂ thin-film solar cell absorbers](#)

[Appl. Phys. Lett.](#) **101**, 103908 (2012); 10.1063/1.4751261

[Comparative atom probe study of Cu\(In,Ga\)Se₂ thin-film solar cells deposited on soda-lime glass and mild steel substrates](#)

[J. Appl. Phys.](#) **110**, 124513 (2011); 10.1063/1.3665723

[Tunneling-enhanced recombination in Cu\(In,Ga\)Se₂ heterojunction solar cells](#)

[Appl. Phys. Lett.](#) **74**, 111 (1999); 10.1063/1.122967

A flatter gallium profile for high-efficiency Cu(In,Ga)(Se,S)₂ solar cell and improved robustness against sulfur-gradient variation

Chien-Yao Huang,^{1,2,a)} Wen-Chin Lee,¹ and Albert Lin²

¹TSMC Solar Ltd., Taichung 42882, Taiwan

²Department of Electronic Engineering, National Chiao-Tung University, Hsinchu 30010, Taiwan

(Received 20 June 2016; accepted 12 August 2016; published online 1 September 2016)

Co-optimization of the gallium and sulfur profiles in pentenary Cu(In,Ga)(Se,S)₂ thin film solar cell and its impacts on device performance and variability are investigated in this work. An absorber formation method to modulate the gallium profiling under low sulfur-incorporation is disclosed, which solves the problem of Ga-segregation in selenization. Flatter Ga-profiles, which lack of experimental investigations to date, are explored and an optimal Ga-profile achieving 17.1% conversion efficiency on a 30 cm × 30 cm sub-module **without anti-reflection coating** is presented. Flatter Ga-profile gives rise to the higher $V_{oc} \times J_{sc}$ by improved bandgap matching to solar spectrum, which is hard to be achieved by the case of Ga-accumulation. However, voltage-induced carrier collection loss is found, as evident from the measured voltage-dependent photocurrent characteristics based on a small-signal circuit model. The simulation results reveal that the loss is attributed to the synergistic effect of the detrimental gallium and sulfur gradients, which can deteriorate the carrier collection especially in quasi-neutral region (QNR). Furthermore, the underlying physics is presented, and it provides a clear physical picture to the empirical trends of device performance, I–V characteristics, and voltage-dependent photocurrent, which cannot be explained by the standard solar circuit model. The parameter “ F_{Ga} ” and front sulfur-gradient are found to play critical roles on the trade-off between space charge region (SCR) recombination and QNR carrier collection. The co-optimized gallium and sulfur gradients are investigated, and the corresponding process modification for further efficiency-enhancement is proposed. In addition, the performance impact of sulfur-gradient variation is studied, and a gallium design for suppressing the sulfur-induced variability is proposed. Device performances of varied Ga-profiles with front sulfur-gradients are simulated based on a compact device model. Finally, an exploratory path toward 20% high-efficiency Ga-profile with robustness against sulfur-induced performance variability is presented. *Published by AIP Publishing.* [<http://dx.doi.org/10.1063/1.4961605>]

I. INTRODUCTION

The Chalcopyrite-based thin film solar cell has emerged as a promising candidate for photovoltaic applications due to its high conversion efficiency headroom, evident from the reported >21% efficiency lab-scale cells^{1,2} by co-evaporation. For large-scale industrial manufacturing, “sulfuration after selenization” (SAS) process of Cu-In-Ga metal precursor to form a pentenary Cu(In,Ga)(Se,S)₂ (CIGSeS) absorber has been a preferred technology for its low cost, friendly production, and uniform deposition.^{3–7} However, there has been a considerable conversion efficiency gap between large-scale CIGSeS modules and lab-scale high-efficiency Cu(In,Ga)Se₂ (CIGS) cells, which needs to be eliminated for realizing the high-efficiency and cost-competitive thin-film photovoltaic.

A notch-shaped gallium profile to form “double-graded bandgap” has been known as an important prerequisite for achieving the record high-efficiency CIGS lab-cells.^{1,4,8–11} A double-graded bandgap profiling consists of wider bandgap regions near the p-n junction and back contact, which effectively reduces the recombination losses. In the case of

selenization process, Ga element tends to segregate, and thus an increased Ga-concentration is resulted toward the Mo back contact. Consequently, the Ga-profile inherently produced by selenization is hard to form the front E_g grading since it requires an increased Ga-concentration toward the p-n junction. A sulfuration step afterward is used to form an increased S-concentration toward the absorber’s surface and build the front E_g grading with a wider bandgap region near the p-n junction. For pentenary Cu(In,Ga)(Se,S)₂ absorbers, the conduction band minimum (CBM), valence band maximum (VBM), and bandgap (E_g) depend on both Ga/(Ga + In) and S/(Se + S) ratios.^{12,13} As Ga/(Ga + In) ratio increases, the E_g of CIGSeS is enlarged by an increased CBM. As S/(Se + S) ratio increases, the E_g of CIGSeS is enlarged by both the increased CBM and decreased VBM. Therefore, “sulfuration after selenization” (SAS) process can produce a CIGSeS absorber with double-graded bandgap by controlling both of the gallium and sulfur profiling.

For the back E_g grading of CIGSeS absorber, the increased CBM and E_g toward the back contact can be designed by a Ga-grading in the sulfur-free Cu(In_{1-x}Ga_x)Se₂ region with tunable bandgaps of 1.04–1.68 eV. For the front E_g grading, a wider E_g region near the p-n junction can be

^{a)}Author to whom correspondence should be addressed. Electronic mail: godlizzandyp@gmail.com

designed by both of the Ga and S contents in $\text{Cu}(\text{In}_{1-x}\text{Ga}_x)(\text{Se}_{1-y}\text{S}_y)_2$ region with tunable bandgaps of 1.04–2.4 eV. The grading of CBM and VBM can also be adjusted by the Ga and S-gradients. Accordingly, the pentenary CIGSeS absorber has higher tunability for bandgap engineering. Nevertheless, the design of composition gradients of CIGSeS cells is more complicated as compared with the lab-scale CIGS cells by co-evaporation. Very few physical studies on the optimal composition profile for pentenary CIGSeS absorber are reported to date.

In practice, Ga-segregation toward the back of absorber during selenization process, which results in the inhomogeneity of films and low V_{oc} , has been widely discussed.^{14–17} Such effect adversely limits the capability of bandgap engineering, and it is regarded as an efficiency limiting factor in CIGSeS technology. Some studies^{4,7,18} found that the enhanced sulfuration degree is a factor in improving the gallium-diffusion toward the surface of absorber. Nevertheless, the gallium and sulfur profiles cannot be co-optimized through this approach. For enhancing gallium-diffusion, sulfuration degree should be substantially increased. However, an increased sulfuration may induce “over-sulfuration” effect^{4,7,18} to cause parasitic resistance losses. The side-effect comes from the excessive sulfur-incorporation, and it deteriorates the efficiency by reducing fill factor (FF). Therefore, low sulfur-incorporation is required for a high-efficiency CIGSeS absorber, and such requirement makes it more difficult to enhance the gallium-diffusion in SAS process.

To date, the lack of theoretical studies and process capability on Ga-profile modulation limits the efficiency improvement of SAS-fabricated CIGSeS solar cells from the optimal bandgap profiling. This deficiency is one of the main causes of the efficiency gap between large-scale CIGSeS modules and lab-scale CIGS cells. Besides, the lack of investigation in performance sensitivity to composition variation leaves an inadequate understanding for improving production yield. These deficiencies hinder the industrial take-off of chalcopyrite thin film photovoltaics. Therefore, a comprehensive understanding of the optimized Ga-profile in CIGSeS solar cells with low sulfur-incorporation and its impacts on performance and variability are very important for the production efficiency enhancement.

A state-of-the-art absorber formation technology has been reported by TSMC Solar demonstrating the previous record 15.7% and 16.5% total-area efficiency on 1.09 m² commercial-sized CIGSeS module.^{19,20} This technology provides a platform to modulate the gallium profile without the need of enhancing sulfuration degree, which avoids parasitic resistances losses by “over-sulfuration.” Through this platform, experimental investigation of the optimal gallium profiling under low sulfur-incorporation can be realized on the pentenary CIGSeS solar cells for the first time. In this work, the experiments of Ga-profile modulation under low sulfur-incorporation are conducted and 17.1% conversion efficiency on a 30 cm × 30 cm CIGSeS sub-module **without anti-reflection coating (ARC)** is achieved. Detailed film properties and related process knobs are disclosed. More importantly, understanding the physical mechanisms that

lead to the improved efficiency can help universal performance and yield enhancement for a variety of CIGSeS formation technology. These samples were characterized by comprehensive material and electrical analysis. Besides, the underlying physics of experimental results is disclosed through analysis and Technology Computer Aided Design (TCAD) simulations. Co-optimization of the gallium and sulfur gradients is investigated, and the corresponding process modification for further efficiency improvement is proposed. Performance variability induced by the sulfur-gradient is also studied. A detailed comparison of the simulation results with the measured device parameters shows that the established TCAD model can reproduce the experimental observations (η , V_{oc} , J_{sc} , FF, J-V, $J_{ph}(V)$, $\eta_c(V)$). Based on the modeling, the device simulations of varied Ga and S-gradients were carried out for path-finding. Finally, a path toward 20% high-efficiency Ga-profile with robustness against sulfur-induced performance variability is presented. This study also pinpoints the importance of gallium-engineering for the higher manufacturing yield of state-of-the-art CIGSeS production lines.

II. EXPERIMENTAL AND CHARACTERIZATION RESULTS

In this work, the layer structure in CIGSeS thin film solar cells is Glass substrate/Mo(Back contact)/CIGSeS(Absorber)/CdS(Buffer)/ZnO:B(Window). Each cell is monolithically interconnected via three scribing patterns (P1, P2, P3) to form a 30 cm × 30 cm sub-module. A 350 nm molybdenum (Mo) thin film was deposited on the glass substrate by DC magnetron sputtering. For monolithic cell integration, a high-power laser was used to scribe the Mo layer and generate the P1 pattern. The P1 pattern defined the unit cell area by isolating each cell in Mo layer. CuGa/In metal alloy layers were deposited by DC magnetron sputtering. The deposited thin film layers form a 340 nm metal precursor with $\text{Ga}/(\text{Ga} + \text{In}) \cong 0.26$ and $\text{Cu}/(\text{Ga} + \text{In}) \cong 0.90$, measured by inductively coupled plasma (ICP) atomic emission spectrometry. Then the precursors were placed in a quartz tube furnace for absorber formation process (chalcogenization). During the furnace process, 1.7 μm CIGSeS absorbers were formed by sequential selenization in H_2Se gas, thermal annealing in N_2 gas, and sulfuration in H_2S gas. Firstly, 70 Torr H_2Se was filled into the furnace at room temperature, and the total pressure was further increased to 650 Torr by filling N_2 gas. When selenization was performed, the furnace temperature was ramped and held at 415 °C for 180 min. At the end of the selenization step, the furnace was purged and filled with N_2 gas. For N_2 annealing process, the furnace temperature was further ramped and held at 540 °C for 30 min (1×) annealing time. Final sulfuration step was performed at 520 °C for 25 min with the mixed gases of H_2S (100 Torr)/ N_2 (550 Torr). In this experiment, the CIGSeS absorbers with different gallium profiling were prepared by adjusting N_2 annealing process. 1×/1.3×/1.4×/1.6×/2× annealing time was applied to samples A, B, C, D, and E for gallium profile modulation, while the other process conditions were kept the same for fair comparison. The average

TABLE I. The composition non-uniformity of samples A, B, C, D, and E measured by X-ray fluorescence (XRF) spectrometer. In all of these samples, the averaged Cu/(Ga + In) ratio is 0.90 with uniform depth-distribution, and the averaged Ga/(Ga + In) ratio is 0.26 with different front-to-back Ga ratios. The averaged composition ratios are measured by inductively coupled plasma (ICP) atomic emission spectrometry.

Sample	Cu/(Ga + In) non-uniformity (%)	Ga/(Ga + In) non-uniformity (%)	Se/(Cu + In + Ga) non-uniformity (%)	S/(Se + S) non-uniformity (%)
A	0.82	0.74	0.81	0.92
B	0.91	0.71	0.84	0.89
C	0.78	0.69	0.72	0.85
D	0.90	0.74	0.75	0.94
E	0.94	0.75	0.77	0.91

elemental compositions of these absorbers such as Cu/(Ga + In), Ga/(Ga + In), and S/(Se + S) were fixed. After the absorber formation process, a 15 nm CdS-based buffer was grown on the absorber layer by chemical bath deposition (CBD) method. The CdS-based buffer was formed by a chemical source of CdSO₄, NH₄OH, and thiourea dissolved in deionized (DI) water for 20 min. Subsequently, a P2 pattern on the buffer layer was generated by a mechanical scribing. The P2 pattern was used to interconnect each unit cell. Afterward, a 1.8 μm ZnO:B transparent conductive oxide was deposited on the buffer layer by metal-organic chemical vapor deposition (MOCVD) method. Finally, the window layer was mechanically cut with a P3 pattern for cell isolation. To avoid overestimating the solar module's conversion efficiency in real-world applications, we did not deposit an anti-reflection coating layer on these modules. In these monolithic modules, the unit cells are connected in series. The single unit cell area was 13.725 cm² with 8% dead-zone region (active area = 12.627 cm²).

To determine a representative composition profile of each sample, we check the composition variation measured by X-ray fluorescence (XRF) spectrometer. In each sample, the elemental composition is measured at 25 different positions with 6 cm × 6 cm spacing. The composition non-uniformity is calculated by the measured 25 data points. As shown in Table I, the composition non-uniformity of these modules is smaller than 1%. Such small variation corresponds to the well-controlled uniformity of the metal precursor deposition and the chalcogenization process.

The composition depth profile of CIGSeS absorber layer is measured by transmission electron microscopy (TEM)-energy dispersive spectroscopy (EDS) with sub-nm depth resolution and calibrated with total elemental composition measured by inductively coupled plasma (ICP) atomic emission spectrometry. The specimens for cross-sectional transmission electron microscopy are mechanically thinned using a dimpler and milled using an Ar ion beam at a liquid N₂ temperature to minimize potential excessive heating and ion beam induced damage. The final thickness of the specimens is approximately 500 Å. TEM analysis is performed using an FEI Tecnai G2 F-20 electron microscope operated at 200 kV. The energy-dispersive spectroscopy (EDS) line scans of the samples are recorded using scanning transmission electron microscope

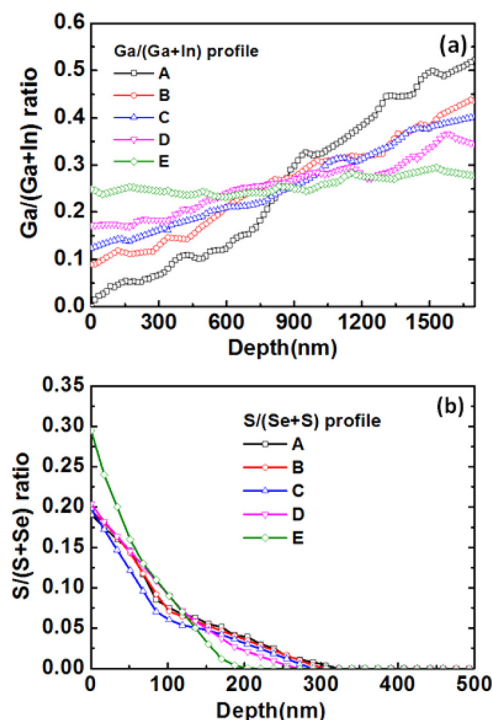


FIG. 1. Ga/(Ga + In) and S/(Se + S) depth profiles by STEM-EDS. (a) Front-to-back Ga ratio “F_{Ga}” for samples A, B, C, D, and E are 0%, 20%, 30%, 50%, and 90%, respectively. (b) S/(Se + S) profiles show comparable concentration among these samples, but the gradients are different. The increased surface S/(Se + S) ratio and decreased penetration depth are observed from samples A to E. Sample E has relatively higher surface S/(Se + S) = 29.5% and shallower penetration depth D_p = 11% than other samples. In all of these samples, the averaged Cu/(Ga + In) ratio is 0.90 with uniform depth-distribution, and the averaged Ga/(Ga + In) ratio is 0.26 with different front-to-back Ga ratios. The averaged composition ratios are measured by inductively coupled plasma (ICP) atomic emission spectrometry.

(STEM) mode. For the quantitative compositional analysis, the spot size for STEM mode is about 0.2 nm. Sample drift is minimized by comparing the STEM image before and after recording the EDS line scan. The system detection error bar is estimated to be ±2%. Because of the uniform composition distribution, we take the EDS line scan of the center region of the sample as the representative depth profile.

The composition depth profiles of Ga/(Ga + In) and S/(Se + S) measured by STEM-EDS are shown in Figs. 1(a) and 1(b). The atomic ratio of Ga/(Ga + In), known as “GGI,” is a critical parameter determining the band gap (E_g) and the conduction band minimum (CBM) of CIGSeS material.^{12,13} Higher GGI in the junction region can lead to the higher bandgap and V_{oc}. For the selenized Cu(In,Ga)Se₂ or Cu(In,Ga)(Se,S)₂ films, Ga-accumulation near the Mo-side has been regard as a fundamental problem to limit the V_{oc}.^{14–17} In this work, the modulation of Ga-gradients is demonstrated by adjusting N₂ annealing process. As shown in Fig. 1(a), gallium profile becomes flatter from sample A to sample E. This shows that longer thermal treatment in nitrogen gas environment can enhance the interdiffusion of Ga and In atoms in the selenized films that has Ga-accumulation problem. Such controllable diffusion property of Ga/In atoms in chalcopyrite structure allows us to optimize the gallium profiling for higher V_{oc}.

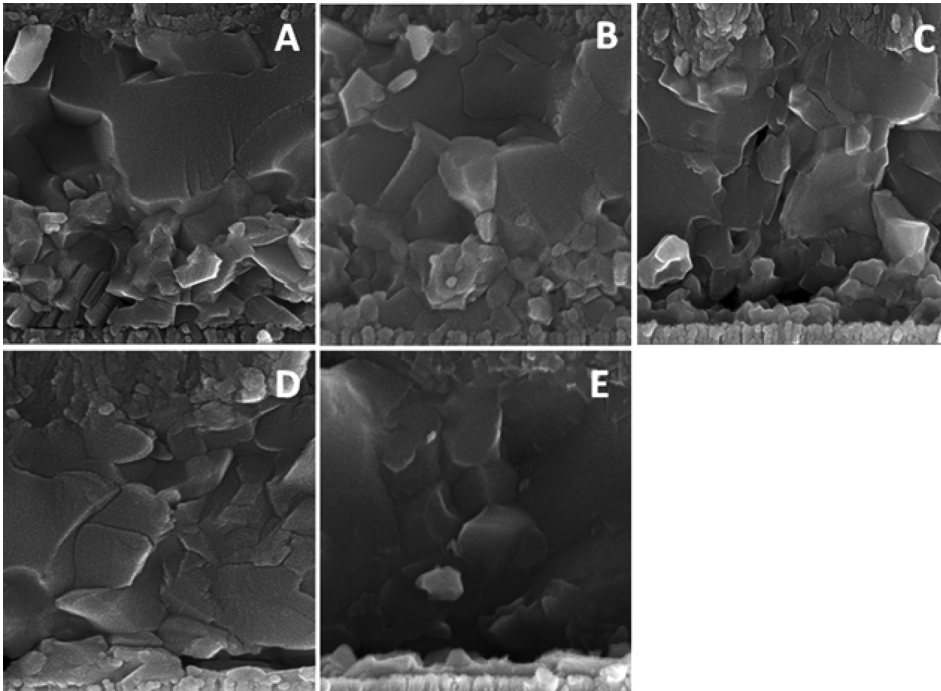


FIG. 2. SEM images of samples A, B, C, D, and E.

Fig. 2 shows the cross section of these absorbers by scanning electron microscope (SEM). In sample A, a large number of small grains form at the bottom side that has higher Ga-concentration, GGI ratio $\cong 0.5$. Lundberg *et al.*²¹ observed the higher Ga-concentration in co-evaporated CIGS films results in smaller grains, which is irrelevant to the sequence of Ga/In layer stacks during chalcogenization. In this work, similar experimental results can be observed in selenized CIGSeS absorbers. From sample A to sample E, the grains in the bottom region become larger with a decreased backside Ga-concentration, which can be adjusted by the N_2 annealing step. This result also shows the recrystallization of chalcopyrite structure during the Ga-In interdiffusion process. In addition, the more homogeneous gallium profiling corresponds to the improved homogeneity of film structures (Fig. 2).

The atomic ratio of $S/(Se + S)$ can affect the E_g , CBM, and VBM of CIGSeS material.^{12,13} As shown in Fig. 1(b), these samples have comparable sulfur-concentration as indicated by the integral of $S/(Se + S)$ profile, but the gradients are different. As the gallium profile is flatter, the surface $S/(Se + S)$ ratio increases, and the penetration depth decreases. According to the published thermodynamic data,²² the formation of Ga_2S is thermodynamically preferred over the formation of In_2S during sulfuration process. It provides a qualitative insight into this experimental observation. The flatter gallium profile has higher GGI ratio near the front side and lower GGI ratio near the backside, which can force more sulfur remaining at the surface due to the preferable reaction of Ga-S rather than In-S. Accordingly, the higher surface Ga-concentration and more homogeneous gallium profile in sample E lead to the relatively higher surface $S/(Se + S)$ ratio and a shallower penetration depth. This finding reveals the thermodynamic interaction between sulfur and gallium distribution, which should be considered in the process tuning.

For quantitative analysis, $Ga/(Ga + In)$ and $S/(Se + S)$ depth profile are described by the specific parameters. Parameter “ Ga_f ” is defined as the front or surface $Ga/(Ga + In)$ ratio at the absorber/buffer interface, while “ Ga_b ” is defined as the back or bottom $Ga/(Ga + In)$ ratio at the absorber/back contact. The parameter “ F_{Ga} ,” which represents “front-to-back Ga ratio” or “surface-to-bottom Ga ratio,” is defined as Ga_f/Ga_b to describe the flatness of GGI depth profile. Therefore, a gallium depth profile in the absorber layer can be described by an “ F_{Ga} ” and an averaged GGI ratio “ GGI_{avg} .” In this work, GGI_{avg} of these samples is fixed at 0.26, and the “ F_{Ga} ” parameters for samples A, B, C, D, and E are 0%, 20%, 30%, 50%, and 90%, respectively. The sulfur profile can be described by a surface $S/(Se + S)$ ratio “SS” and a normalized penetration depth “ D_p .” The corresponding parameters for samples A, B, C, D, and E are listed in Table II. As mentioned above, sample E has relatively higher surface $S/(Se + S) = 29.5\%$ and shallower penetration depth $D_p = 11\%$ than other samples. These quantitative indices show that our absorber formation method can produce a wide range of gallium-gradients ($F_{Ga} = 0\% - 90\%$) under a fixed sulfur-incorporation. The interaction between gallium and sulfur gradients during the absorber formation process is also observed.

The minority carrier lifetime “ τ_n ” of CIGSeS absorber is determined by Time-Resolved Photoluminescence (TRPL). For measuring the carrier lifetime of the bare absorber, the CdS and ZnO:B layers are removed by diluted HNO_3 . For TRPL, the detection wavelength is set to the photoluminescence (PL) maximum, and a near infrared fluorescence lifetime spectrometer with 532 nm laser is used to measure the PL decay curve. Due to the high absorption coefficient ($\sim 10^5 \text{ cm}^{-1}$) of chalcopyrite materials, incident photons can be completely absorbed by the front 400 nm-thick CIGSeS absorber. Therefore, the extracted carrier lifetime by TRPL is determined by the recombination process in the front

TABLE II. Material properties and device characteristics of samples A, B, C, D, and E.

Sample	F_{Ga} (%)	SS (%)	D_{p} (%)	τ_{n} (ns)	2Θ (deg)	$E_{\text{g,min}}$ (eV)	J_0 (mA/cm ²)	A-	R_{s} (Ω cm ²)	R_{sh} (Ω cm ²)
A	0	19.1	18	10.5	26.85	1.03	1.7×10^{-6}	1.44	0.94	1438
B	20	19.6	17	10.5	26.95	1.07	1.2×10^{-6}	1.40	0.86	1453
C	30	19.8	16	10.6	26.97	1.08	9.1×10^{-7}	1.35	0.94	1560
D	50	20.4	15	10.2	27.05	1.10	3.3×10^{-7}	1.33	0.90	1450
E	90	29.5	11	10.9	27.13	1.12	4.9×10^{-8}	1.31	0.92	1550

absorber, and it can be affected by the physical properties that vary with composition grading such as bandgap, defects, carrier density, etc. From sample A to sample E, the increased Ga/(Ga + In) and S/(Se + S) near the absorber's surface can contribute to higher E_{g} , and hence a higher carrier lifetime is expected. Nonetheless, the extracted carrier lifetime from all of these samples is limited to be around 10 ns (Table II). The limited carrier lifetime is attributed to the degradation of CIGSeS films, which has been observed in our fabrication environment. The degradation of the bare absorber has also been observed and reported by several groups. National Renewable Energy Laboratory (NREL) reported that the carrier lifetime degrades fast as the bare absorber is exposed to the non-vacuum environment.²³ The degradation of carrier lifetime corresponds to the increased carrier recombination by the formation of defects. In this work, the time period between SAS and CBD processes that we can control is around 5 hours. Therefore, the prepared CIGSeS samples were degraded by the air-exposure. Because of the increased recombination, the measured carrier lifetime of these samples was limited to be around 10 ns. A method that has been known to avoid the degradation is to deposit the CdS layer as soon as the absorber is removed from the vacuum chamber. After CdS deposition, samples are stable in air for months. Therefore, the time control between SAS and CBD processes is an approach for further efficiency-improvement. More importantly, NREL demonstrated that once the degraded absorbers are made into complete devices, the device performance is strongly correlated to the measured TRPL lifetime of degraded films.²³ The study supports that the measured TRPL lifetime in this work is physically meaningful and can be factored in the analysis of device performance.

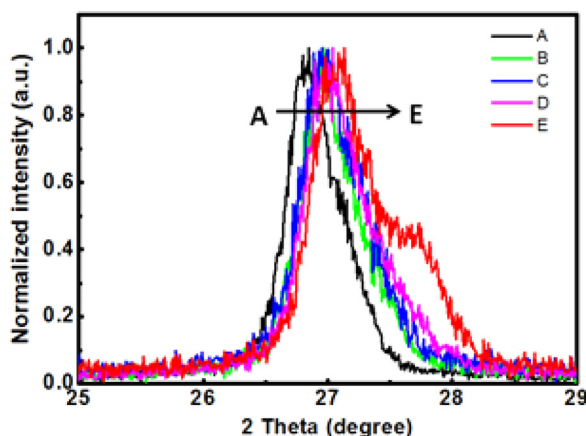


FIG. 3. GIXRD patterns of CIGSeS (112) peak position with 0.5° incident angle.

Glancing incident angle X-ray diffraction (GIXRD) is also used to analyze the bare CIGSeS absorber. In GIXRD analysis, a 0.5° incident angle is set to analyze the surface region of the absorbers. As shown in Fig. 3, the shift of (112) peak position toward the higher 2theta angle “ 2Θ ” from sample A to sample E corresponds to an increased F_{Ga} . Quantum efficiency (QE) of complete device is measured as shown in Fig. 4. Minimum bandgap ($E_{\text{g,min}}$) is extracted by calculating the bandgap energy from the long wavelength where a 30% QE value is observed. Dark J-V characteristics are measured as shown in Fig. 5(a). Diode saturation current density (J_0), ideal factor (A), series resistance (R_{s}), and shunt resistance (R_{sh}) are extracted from measured J-V curves according to Ref. 24. Illuminated J-V characteristics as shown in Fig. 5(a) are measured at standard test condition (STC) (AM1.5G intensity and room temperature). The corresponding performance parameters are extracted as shown in Figs. 6(a)–6(d). The film properties and device characteristics mentioned above are summarized in Table II.

Notably, the comparable R_{s} and R_{sh} in these samples indicate that the flatter Ga-profiles produced by this work do not induce “over-sulfuration” effect, which can cause severe parasitic losses. Due to the separate engineering of gallium and sulfur profiles in the absorber formation platform, no excessive sulfur-incorporation is needed to enhance the gallium-diffusion. This distinguishing property allows us to investigate the effect of Ga-profile modulation and its intrinsic impact on device performance, which lacks the experimental investigation for pentenary Cu(In,Ga)(Se,S)₂ photovoltaics.

From sample A to sample E, the flatter Ga-profile, i.e., an increased F_{Ga} , means higher Ga-concentration in the front of the absorber layer. In CIGSeS absorbers, the higher Ga-

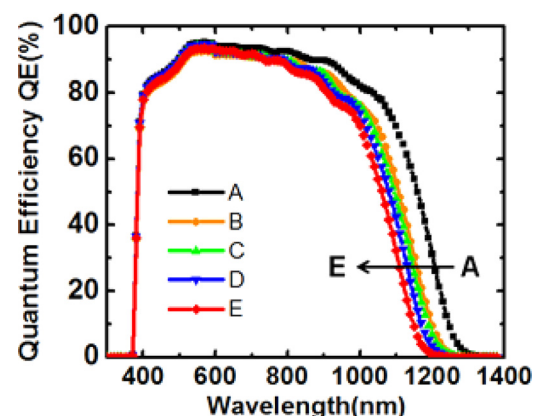


FIG. 4. Quantum efficiency vs. wavelength of samples A, B, C, D, and E.

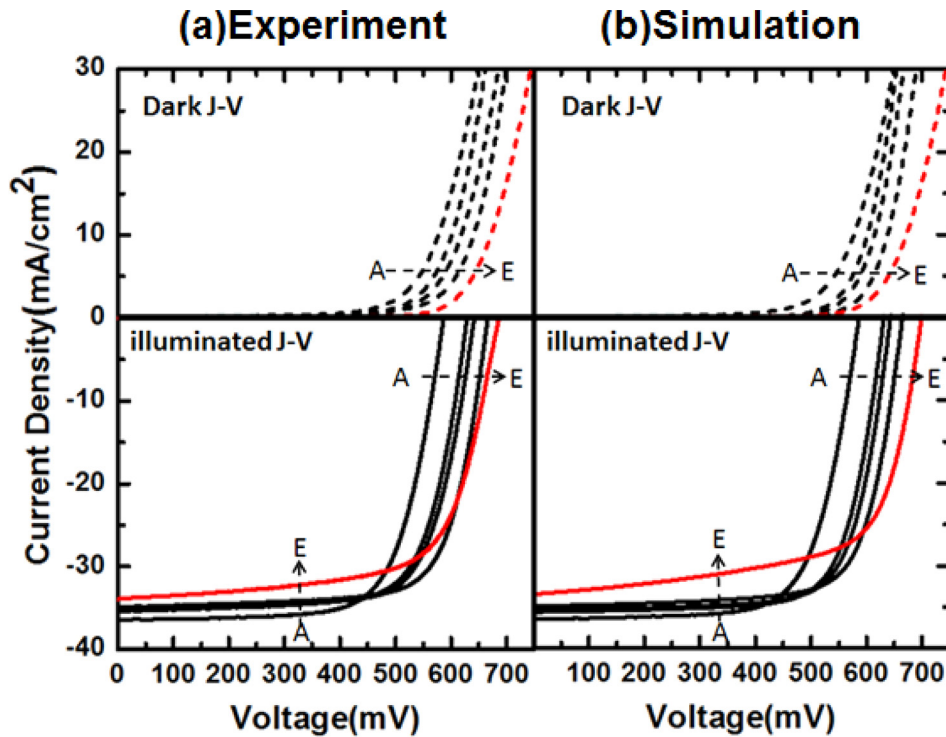


FIG. 5. Illuminated and dark J-V characteristics of samples A, B, C, D, and E: (a) Experiment. (b) Simulation. The arrows indicate the respective shift from samples A to E. J-V curves of sample E are marked in red and show serious distortions under illumination.

incorporation can lead to the improved bandgap. As shown in Fig. 4, an increased F_{Ga} (0%–90%) enlarges the absorber’s minimum bandgap ($E_{g, min}$) from 1.03 eV to 1.12 eV. Such high $E_{g, min}$ is demonstrated under the constraint of low $G_{GI, avg}$ (26%) and SS (30%). In addition, the bandgap of the regions near p-n junction is improved, as evidenced by the increased peak position (26.85° to 27.13°) of (112) chalcopyrite phase in GIXRD analysis. Remarkably, sample E with $F_{Ga} = 90\%$ shows a second peak position of 27.75° (Fig. 3). Such high peak position reveals the phase formation of Ga-

rich $Cu(In,Ga)(Se,S)_2$. These two peaks in GIXRD indicate the phase separation of CIGSeS, which can form structure defects. The induced defects near the junction may cause severe recombination loss. On the other hand, Ga-rich CIGSeS phase can enlarge the bandgap near the junction, which can reduce carrier recombination. For the formation of Ga-rich CIGSeS, the combination of these two induced effects determines its impact on device performance. Among these samples, sample E shows the best V_{oc} , A, and J_0 (Table II and Fig. 6(c)), which indicates that its diode quality is the

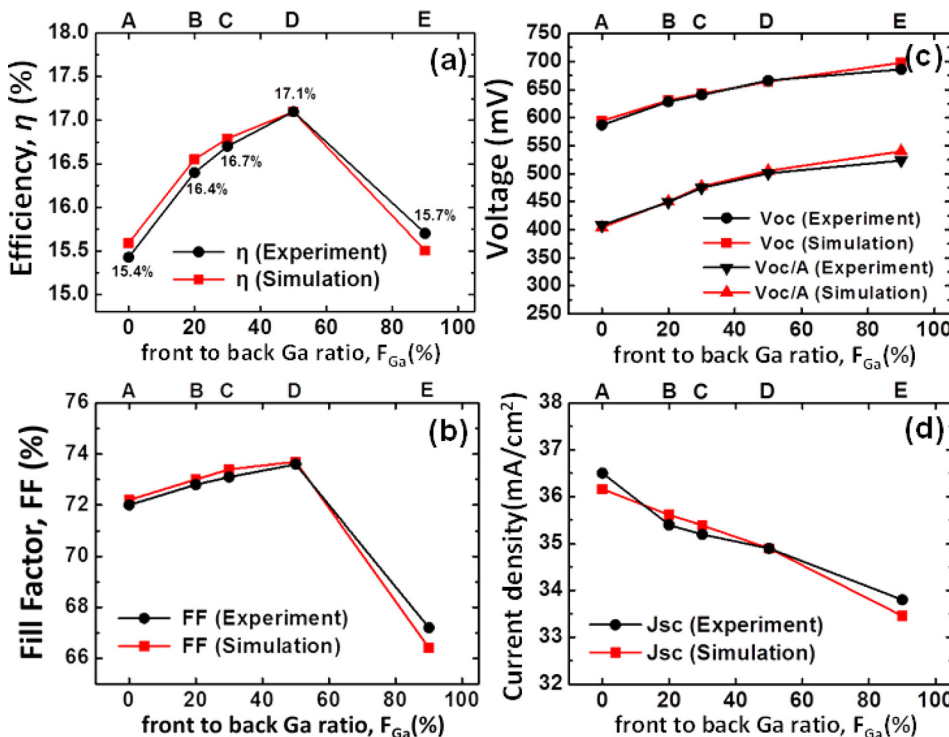


FIG. 6. Device performance parameters vs. F_{Ga} : (a) conversion efficiency η , (b) fill factor FF, (c) V_{oc} and V_{oc}/A , and (d) J_{sc} . The measured parameters are marked in black, and the simulated parameters are marked in red.

highest. These performance results show that the carrier recombination is dominated by the enlarged bandgap rather than the induced defects. Therefore, the effect of an enlarged bandgap is more pronounced than the effect of the phase separation induced defects. Overall, these results reflect effective Ga-incorporation during the absorber formation, and thus it builds a strong correlation between the parameter F_{Ga} , (112) peak position (2Θ), and bandgap shift (E_g) (Table II). This correlation shows that the thermal budget of N_2 annealing step is an effective process knob for bandgap tuning.

For a chalcopyrite-based solar cell, there are three possible carrier recombination paths: (1) space charge region (SCR) recombination, (2) quasi-neutral region (QNR) recombination, and (3) absorber/buffer interface recombination. These paths contribute to the total recombination current under forward bias. Increased F_{Ga} can improve the bandgap near the junction, and thus it reduces the recombination loss in space charge region (SCR). On the other hand, increased F_{Ga} causes more recombination losses in quasi-neutral region (QNR) due to the narrowed bandgap and the reduced back electric field. Based on the measured results, the significant reduction in saturation current J_0 with increased F_{Ga} (Table II) indicates that the dominant recombination path in these devices takes place in SCR rather than QNR. From the viewpoint of conduction band offset (CBO), more gallium at the absorber's surface can increase the CBM and change spike-like CBO to cliff-like CBO, which blocks electron transportation across the buffer/absorber interface to trigger strong interface recombination. By calculating the CBO followed by Refs. 12 and 13, the conduction band of these samples with surface $\text{S}/(\text{Se} + \text{S})$ ratio = 0.2–0.3 and $\text{Ga}/(\text{Ga} + \text{In})$ ratio = 0–0.25 is spike-like rather than cliff-like junction. By measurement, the continuous J_0 reduction with increased F_{Ga} also supports the fact that no significant interface recombination is activated by a cliff-like junction. Accordingly, saturation current of these devices is most likely dominated by SCR recombination. Besides, the decreased ideal factor toward $A = 1$ indicates that the dominant recombination path shifts toward QNR as F_{Ga} increases.

The experimental results (Fig. 6(a)) show that the flatter Ga-profiles ($F_{\text{Ga}} > 0$) are beneficial to conversion efficiency, as compared with the accumulated Ga-profiles ($F_{\text{Ga}} = 0$). It is remarkable that 17.1% conversion efficiency with $V_{\text{oc}} = 668$ mV, $J_{\text{sc}} = 34.9$ mA/cm², and $\text{FF} = 73.6\%$ is achieved on a 30 cm × 30 cm sub-module **without anti-reflection coating (ARC)**. This significant gain highlights the efficiency headroom from Ga-diffusion enhancement in CIGSeS technology, which has not been reported to date.

Fig. 6 shows the trend of performance parameters with varied F_{Ga} . From sample A to sample E, the short circuit current J_{sc} (Fig. 6(d)) is decreased from 36.5 to 33.8 mA/cm². The observed trend is attributed to the long-wavelength absorption loss as a consequence of wider optical bandgap ($E_{g, \text{min}}$) by increased F_{Ga} , which is confirmed by the blue-shift of QE response edge (Fig. 4). Based on the above analysis, saturation current in these devices is mainly affected by SCR recombination, which can be modulated by the bandgap in the front absorber region. Therefore, the modulation of F_{Ga} is critical for the saturation current reduction. With

increased F_{Ga} (0%–90%), wider bandgap in SCR can lead to significant J_0 reduction by two orders of magnitude from 1.7×10^{-6} to 4.9×10^{-8} mA/cm², which is responsible for the improved open circuit voltage V_{oc} from 587 to 686 mV (Fig. 6(c)). Overall, the $V_{\text{oc}} \times J_{\text{sc}}$ product increases with increasing F_{Ga} because the V_{oc} improvement by reduced carrier recombination is larger than the J_{sc} loss by less optical absorption. In conclusion, from the accumulated Ga-profiles ($F_{\text{Ga}} = 0$) to the flatter Ga-profiles ($F_{\text{Ga}} > 0$), the match between bandgap profiling and solar spectrum gives rise to considerable $V_{\text{oc}} \times J_{\text{sc}}$ improvement.

Increased conversion efficiency by increased F_{Ga} is expected due to the significant $V_{\text{oc}} \times J_{\text{sc}}$ improvement. Surprisingly, the efficiency does not follow such trend and peaks at $F_{\text{Ga}} = 50\%$ (sample D) instead. As shown in Fig. 6(b), the optimal F_{Ga} for the maximum efficiency is determined prominently by the trend of fill factor (FF). In general, FF can be described by the standard solar circuit model²⁵ which can be expressed in terms of V_{oc} , ideal factor A , and parasitic resistances. Accordingly, the increased V_{oc}/A from sample A to sample E as shown in Fig. 6(c) should lead to an increased FF. However, sample E shows a deterioration on FF and conversion efficiency, which cannot be explained by the standard model. Although flatter Ga-profile ($F_{\text{Ga}} > 0$) shows a good prospect for $V_{\text{oc}} \times J_{\text{sc}}$ improvement, efficiency loss may result from the deteriorated FF. To understand the above empirical results, we perform a comprehensive analysis in Sections III, IV, and V.

III. VOLTAGE-DEPENDENT PHOTOCURRENT MEASUREMENT AND ANALYSIS

Based on measured J-V characteristics (Fig. 5(a)), the deteriorated FF on sample E corresponds to the increased slope of dJ/dV in illuminated J-V curve. Nevertheless, the distortion cannot be interpreted by leakage shunting paths in the device, which shows high shunt resistance ($\sim 1550 \Omega \text{ cm}^2$) in the dark J-V curve. The distortion reveals the failure of superposition principle²⁶ that assumed the illuminated J-V curve of a junction should be the same as the dark J-V curve, only shifted downwards by a constant photocurrent. Some studies^{27–30} proposed voltage-dependent photocurrent to interpret such failure of superposition. To quantitatively confirm this model in our experiment, accurate measurement of voltage-dependent photocurrent $J_{\text{ph}}(V)$ is performed based on a small-signal circuit model incorporated with voltage-dependent photocurrent characteristics. The corresponding small-signal model under AC light source is shown in Fig. 7(a). When an AC light source is applied to a solar cell, it produces a small signal photocurrent which acts as an AC current source $j_{\text{ph}}(V')$. The induced small change in voltage/current is considered as a small perturbation at fixed DC bias point. With the small perturbation, the diode acts as a “small-signal resistance r_d .” Using the Shockley equation $I = I_0 \times \exp(qV/AV_T - 1)$, the small-signal resistance r_d can be derived by $(dI/dV)^{-1}$ at fixed DC bias point and expressed as $r_d = AV_T/(I + I_0)$. In this expression, A is diode's ideal factor, V_T is thermal voltage, I is the diode DC output current, and I_0 is the diode saturation current. Parasitic

resistances (R_s and R_{sh}) are also considered in the small-signal circuit model. Using Kirchhoff's law, the small-signal output current $j(V)$ at applied DC voltage-bias V is derived

$$j(V) = \frac{j_{ph}(V')}{\left(\frac{R_s}{r_d} + \frac{R_s}{R_{sh}} + 1\right)}, \quad (1)$$

where $j_{ph}(V')$ is the small-signal photocurrent at DC voltage-bias V' that represents the voltage drop across the p-n junction. R_s is the series resistance, R_{sh} is the shunt resistance, and r_d is the small-signal diode resistance. The DC voltage-bias V' across p-n junction is determined by $V' = V - IR_s$, where V is the applied DC voltage bias at terminals, and I is the DC output current. Based on the small-signal model, voltage-dependent photocurrent $J_{ph}(V)$ can be measured by an AC monochromatic light source, an I-V converter, a lock-in amplifier system, and a DC voltage-bias system. For $J_{ph}(V)$ measurement, devices are placed on a temperature-controlled plate at 25 °C. An AC monochromatic light source is used to excite photo-generated carriers with a frequency of 100 Hz. The small-signal photocurrent $j_{ph}(V')$ generated by these photo-carriers flows from the p-n junction to the terminals and forms a small-signal output current signal. The small-signal output current $j(V)$ is measured over an I-V converter and followed by a lock-in amplifier system for better AC signal accuracy. The $j(V)$ under varied light wavelength illumination is measured and then weighted with AM1.5G solar spectrum to obtain the photocurrent J_{ph} under STC.

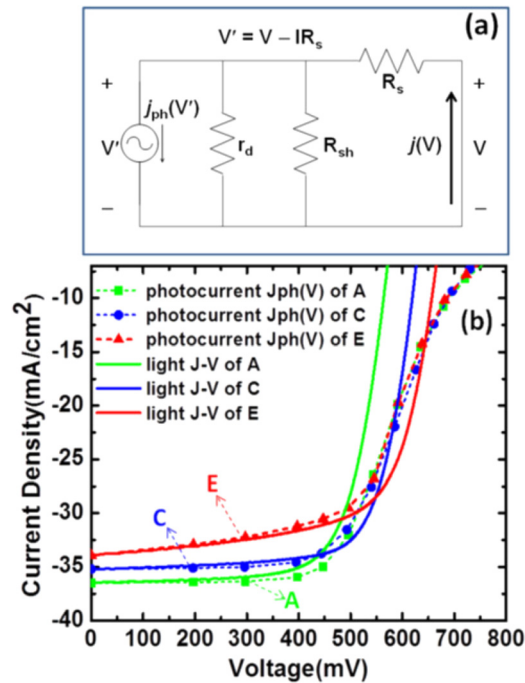


FIG. 7. (a) Small-signal circuit model of a solar cell under AC light source. Voltage-dependent photocurrent characteristic is incorporated. $j(V)$ is the small signal output current at applied DC voltage-bias V . $j_{ph}(V')$ is the small signal photocurrent at DC voltage-bias V' across p-n junction, R_s is the series resistance, R_{sh} is the shunt resistance, and r_d is the small signal diode resistance. The DC voltage-bias V' across p-n junction is determined by $V' = V - IR_s$, V is the applied DC voltage bias at terminals. I is the DC output current. (b) Measured photocurrent $J_{ph}(V)$ (dashed line) and illuminated J-V curves (solid line) of samples A, C, and E.

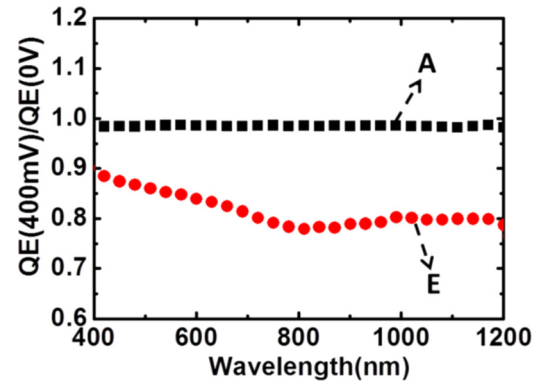


FIG. 8. The measured ratio of $QE(400\text{mV})/QE(0\text{mV})$ for samples A and E. $QE(400\text{mV})$ and $QE(0\text{mV})$ represent measured quantum efficiency at voltage bias = 400 mV and 0 mV, respectively. Sample E shows the reduced ratio of $QE(400\text{mV})/QE(0\text{mV})$, especially at long wavelengths.

Here varied DC voltage-biases are applied on samples A, C, and E to measure the voltage-dependent photocurrent $J_{ph}(V)$ as shown in Fig. 7(b). The ratios of R_s/R_{sh} in these samples are below 10^{-3} and thus can be neglected in Equation (1). At the applied DC voltage-bias $V < 400\text{mV}$, $R_s/r_d (< 10^{-2})$ can be neglected due to large small-signal diode resistance r_d . In addition, the DC voltage-bias V' across p-n junction is close to V due to the negligible DC output current at dark and small DC bias. Therefore, measured photocurrent $J_{ph}(V)$ at terminals is close to the actual photocurrent generated from the p-n junction, $j(V) \cong j_{ph}(V')$. As shown in Fig. 7(b), measured $J_{ph}(V)$ curves match the illuminated J-V curves with distortions in the bias range $< 400\text{mV}$ and thus confirm the voltage-dependent photocurrent characteristics of these samples. As DC voltage-bias V exceeds 400 mV, the exponential growth of diode dark current significantly decreases the small-signal resistance r_d . As a result, the non-negligible term R_s/r_d causes severe decay of the measured photo-current $j(V)$ according to Equation (1). At DC voltage-bias $V > 400\text{mV}$, small-signal diode resistance r_d is less than $100\ \Omega$ and the term R_s/r_d becomes non-negligible ($> 10^{-2}$). Consequently, the measured $J_{ph}(V)$ curves drop exponentially and converge as the applied DC voltage-bias V increases. Based on the measured data, the loss of $J_{ph}(V)$ increases from sample A to sample E and matches the distortion of light J-V curves. Therefore, we can conclude that stronger voltage-dependence on photocurrent drives the FF drop. For further investigation on the $J_{ph}(V)$ loss, the ratio of quantum efficiency response at voltage bias = 400 mV over the response at 0 V is measured as shown in Fig. 8. The measured ratio represents voltage-induced difference on the QE response. Sample E shows reduced QE response under forward bias as indicated by the measured ratio ≤ 1 , and the ratio is lower at long-wavelengths. This indicates that the $J_{ph}(V)$ loss may correlate to the voltage-induced carrier collection loss, especially for carriers generated by long-wavelength photons.

IV. TCAD MODELING

Several models of voltage-dependent photocurrent have been reported based on non-graded bandgap structure.^{31–42}

In the complicated Cu(In,Ga)(Se,S)₂ thin film solar cell, drift and diffusion carrier transportations in both SCR and QNR should be considered with graded bandgap structure. To solve this issue and to provide a clear physical picture, Technology Computer Aided Design (TCAD) simulation is used for compact device modeling by solving coupled device equations of optical, electrostatic, and continuity.

Material parameters of pentenary Cu(In_{1-x}Ga_x)(Se_{1-y}S_y)₂ compounds are determined by interpolation between the four quaternary side materials (CuIn(Se_{1-y}S_y)₂, CuGa(Se_{1-y}S_y)₂, Cu(In_{1-x}Ga_x)Se₂, and Cu(In_{1-x}Ga_x)S₂) based on an interpolation scheme method.^{43,44} Material parameters of this pentenary compound as function of Ga/(Ga + In) and S/(Se + S) ratios can be expressed as below

$$P(x, y) = \frac{1}{x(1-x) + y(1-y)} \times \{x(1-x)\{yP[\text{CuIn}_{1-x}\text{Ga}_x\text{S}_2] + (1-y)P[\text{CuIn}_{1-x}\text{Ga}_x\text{Se}_2]\} + y(1-y)\{xP[\text{CuGa}(\text{Se}_{1-y}\text{S}_y)_2] + (1-x)P[\text{CuIn}(\text{Se}_{1-y}\text{S}_y)_2]\}\}, \quad (2)$$

where $P(x, y)$ represents material parameters of Cu(In_{1-x}Ga_x)(Se_{1-y}S_y)₂ compound, x is the ratio of Ga/(Ga + In), and y is the ratio of S/(Se + S). In this simulation, the bandgap (E_g), conduction band minimum (CBM), valence band maximum (VBM), and optical n, k are interpolated based on the specific Ga/(Ga + In) and S/(Se + S) ratios, while the other parameters remain constant. To determine the bandgap with varied composition, an empirical equation in Ref. 45 can be used. Here, the four quaternary materials are constructed by the ternary corner materials (CuInSe₂, CuGaSe₂, CuInS₂, and CuGaS₂) with zero bowing factors based on experiments.⁴⁶ The bandgap and band offset of these four ternary corner materials are based on first-principle calculations.^{12,13} The bandgaps of Cu(In,Ga)(Se,S)₂ absorber with varied Ga/(Ga + In) and S/(Se + S) ratios used in this simulation are shown in Fig. 9. The optical parameters (n, k values) are extracted from measurement data,^{47,48} and the absorption edges are shifted with varied optical bandgaps. Carrier lifetime of the CIGSeS absorbers is set to 10 ns based on TRPL measurements (Table II). Electron and hole mobility are set to 100 cm² V⁻¹ s⁻¹ and 25 cm² V⁻¹ s⁻¹, respectively, which are in the typical range of polycrystalline chalcopyrite materials.^{49,50} The effective

donor-like defect states in p-type absorber layer are assigned to a narrow Gaussian distribution close to the middle of bandgap (mid-gap states). The capture cross-section for electron/hole (σ_e/σ_h) is set to $5 \times 10^{-13}/1 \times 10^{-15}$ cm².⁵⁰ Here effective defect density = 10^{15} cm⁻³ is used to fit the measured J-V characteristics in experiments. Other material parameters are taken from the standard chalcopyrite thin film solar cell in Ref. 50.

CIGSeS device structure with different Ga and S profiles in samples A, B, C, D, and E as shown in Figs. 1(a) and 1(b) are modeled with the corresponding material parameters mentioned above. The parasitic resistances R_s and R_{sh} coupled in simulations are set to 0.9 and 1500 Ω cm²/cell, respectively, which are the average of extracted resistances as shown in Table II. For optical absorption simulation, transfer matrix method (TMM) is used. By this method, reflection, absorption, and transmission spectra of multilayer stacks are obtained by multiplication of thin film layer matrices. This yields an overall transfer matrix for all wavelengths of interest. For J-V characteristics simulations, optical generation profiles under AM1.5G solar spectrum are calculated by transfer matrix method (TMM), and the following electrical simulation is responsible for solving coupled Poisson and continuity equations at varied voltage biases. Recombination models (Shockley-Read-Hall (SRH), Auger, Radiative, and surface recombination) are also incorporated. The respective performance parameters are derived from the simulated J-V characteristics.

To analyze voltage-dependent photocurrent characteristics, voltage-dependent carrier collection efficiency $\eta_c(V)$ is defined according to $J_{ph}(V) = J_{sc}\eta_c(V)$. Carrier collection efficiency is referred to as the probability that a photo-generated carrier inside the device is collected at terminal contacts. The voltage-dependent carrier collection efficiency $\eta_c(V)$ represents the voltage-induced difference in carrier collection efficiency with a specific carrier generation profile. $\eta_c(V)$ can be estimated from the difference between J-V characteristics with differing illumination according to Ref. 30

$$\eta_c(V) \cong \frac{\frac{\Delta \text{collected carriers}(V)}{\Delta \text{generated carriers}}}{\frac{\Delta \text{collected carriers}(0V)}{\Delta \text{generated carriers}}} \cong \frac{J_{I1}(V) - J_{I2}(V)}{J_{sc,I1} - J_{sc,I2}}, \quad (3)$$

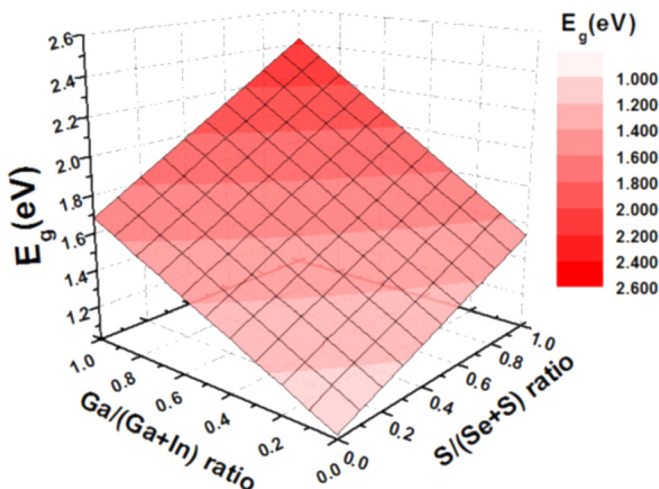


FIG. 9. The bandgap (E_g) of pentenary Cu(In_{1-x}Ga_x)(Se_{1-y}S_y)₂ material with varied Ga/(Ga + In) and S/(Se + S) ratios based on the interpolation scheme method.

where $J_{sc,I}(V)$ and $J_{sc,I2}(V)$ represent the short-circuit current under differing illumination, and $J_{I1}(V)$ and $J_{I2}(V)$ represent the J-V characteristics under differing illumination. Localized voltage-dependent carrier collection efficiency $\eta_c(x,V)$ is defined as voltage-dependent carrier collection efficiency at a given location x with a carrier generation $G(x)$. Here $\eta_c(x,V)$ profile is simulated by artificially creating additional carrier generation $\Delta G(x)$ at a location x and calculating the output current difference according to Equation (3). The integral of $\eta_c(x,V)$ profile and optical generation profile $G(x)$ under AM1.5G illumination is equal to $\eta_c(V)$ of the whole device. In $\eta_c(V)$ and $\eta_c(x,V)$ simulations, series resistances are set to zero to make the output voltage (V) equal to the voltage-bias across junction (V'). This equality allows us to simulate actual collection efficiency, especially at high voltage bias.³⁰

V. DISCUSSIONS

Simulated J-V characteristics in dark and under AM1.5G spectrum are shown in Fig. 5(b). The simulated and measured J-V curves with distortions are in good agreement. In addition, the simulated device parameters (η , V_{oc} , FF, and J_{sc}) are well-matched to the measurements in Figs. 6(a)–6(d). The matching indicates that the device performance is indeed dominated by the bandgap profiling (Ga and S profiles) in different samples (Fig. 1) rather than other material properties, such as defects, carrier lifetime, mobility, etc. To further understand the influences of composition grading (F_{Ga} and sulfur-gradient) on device characteristics, the relationship between E_g , CBM, VBM, and composition grading is studied. In CIGSeS absorbers, increased F_{Ga} can result in the increased E_g and CBM in the front of the absorber, the decreased E_g and CBM in the back of absorber, as well as the decreased conduction band grading. The increased front

sulfur-gradient can enlarge the E_g near the surface of absorber by decreased VBM and increased CBM, as well as the grading of the front energy barrier. As a result, the evolution of E_g profiling from sample A to sample E leads to wider E_g near the p-n junction, reduced back E_g grading, and enlarged front energy barrier. The corresponding device characteristics are discussed as below.

A. Origin of voltage-dependent carrier collection

In this work, the voltage-dependence on carrier collection was observed and confirmed by the $J_{ph}(V)$ measurement (Fig. 7(b)). Fig. 10(a) shows the simulated voltage-dependent collection efficiency $\eta_c(V)$ curves which are in good agreement with the measured $J_{ph}(V)$ characteristics. Simulation reveals that the change of composition grading from sample A to sample E degrades the carrier collection under a forward bias. Moreover, the difference in collection efficiency among these samples becomes larger as voltage-bias increases. The collection efficiency at the maximum power point $\eta_c(V_{mpp})$ is simulated as shown in Fig. 10(b). From sample A to sample D, $\eta_c(V_{mpp})$ decreases linearly with increasing F_{Ga} . For sample E, the further increased F_{Ga} and sulfur gradient cause a severe $\eta_c(V_{mpp})$ drop.

To further study the $\eta_c(V_{mpp})$ loss, the localized collection efficiency profiles $\eta_c(x,V_{mpp})$ are simulated for varied F_{Ga} with two kinds of sulfur-gradients, S_L and S_U . Here S_L represents the sulfur profile of sample A, which is the lower bound of measured sulfur-gradients. S_U represents the sulfur profile of sample E, which is the upper bound of measured sulfur-gradients. As shown in Figs. 10(c) and 10(d), the simulated results reveal that the $\eta_c(V_{mpp})$ loss mainly comes from the deteriorated collection efficiency in QNR. An increased F_{Ga} can degrade the collection efficiency because the lower Ga-gradient reduces the CBM grading which can

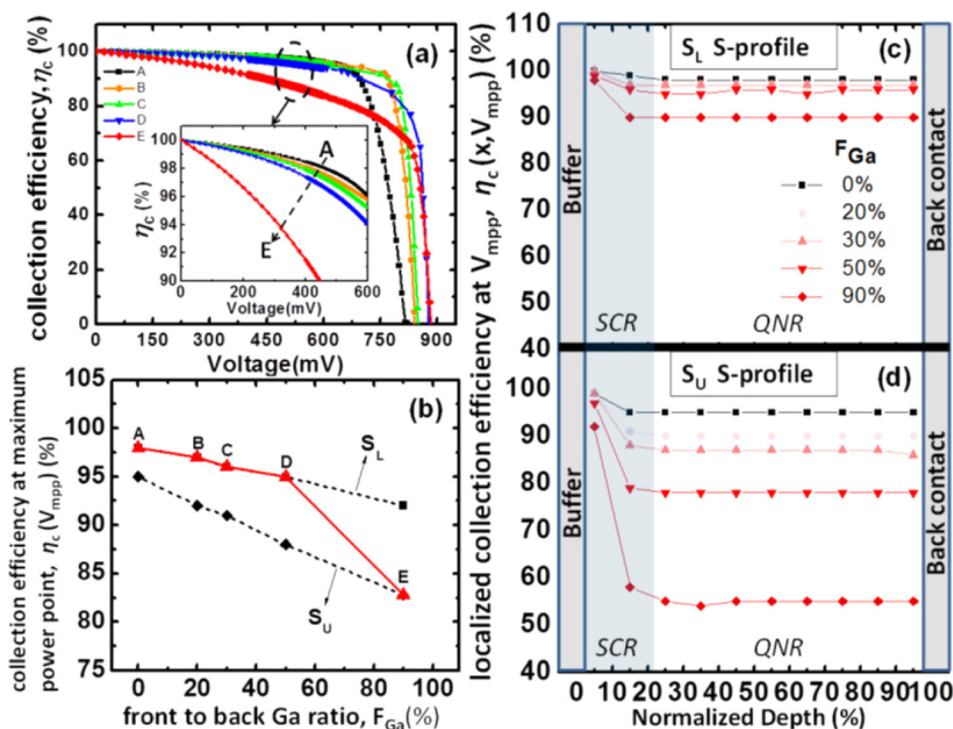


FIG. 10. (a) Simulated voltage-dependent collection efficiency $\eta_c(V)$ curves. The inset shows more $\eta_c(V)$ loss from samples A to E, which is indicated by the dashed arrow. (b) Simulated collection efficiency at the maximum power point $\eta_c(V_{mpp})$ vs. F_{Ga} with S_U and S_L sulfur-gradients. S_L represents the sulfur profile of sample A, which is the lower bound of measured sulfur-gradients. S_U represents the sulfur profile of sample E, which is the upper bound of measured sulfur-gradients. At the maximum power point, the localized collection efficiency $\eta_c(x, V_{mpp})$ profiles with two kinds of sulfur-gradients (S_U and S_L) are simulated as shown in (c) and (d).

force the collection of photo-generated electrons. The degradation of carrier collection is more severe in QNR due to the lack of p-n junction field. By comparing Figs. 10(c) and 10(d), it appears that the increased sulfur-gradient from S_L to S_U also degrades the collection efficiency, especially in QNR. Furthermore, the synergistic effect is found that the $\eta_c(V_{mpp})$ loss by increased sulfur-gradient is more severe as F_{Ga} increases, as shown in Fig. 10(b). Based on the simulated results, the loss of localized collection efficiency is analyzed quantitatively. From sample A to sample E, it is found that an increased F_{Ga} (from 0% to 90%) reduces the collection efficiency from 98% to 90% in QNR (Fig. 10(c)). Additionally, the higher sulfur-gradient on sample E further degrades the collection efficiency to 55% in QNR (Fig. 10(d)), which is attributed to the blocked electron collection by the higher energy barrier. For sample E, the synergistic effect of increased F_{Ga} and sulfur-gradient incurs a large $\eta_c(V_{mpp})$ drop (Fig. 10(b)). Based on the above study, we can conclude that the change of composition grading from sample A to sample E, which leads to the reduced CBM grading and enlarged front energy barrier, is detrimental to the photo-generated carrier collection especially in QNR. We also can understand the decreased long-wavelength quantum efficiency from sample A to sample E (Fig. 4) is resulted from the poor collection of photo-generated electrons in QNR. Moreover, the simulated results corroborate the correlation between the $J_{ph}(V)$ distortion and forward-bias induced carrier collection loss in QNR. The loss of localized carrier collection efficiency mainly occurs in QNR which lacks p-n junction field. As the voltage-bias increases, the wider QNR causes more collection losses in solar cell. Therefore, worse $J_{ph}(V)$ distortion is observed at large forward-bias (Figs. 7 and 10(a)). In addition, the composition grading significantly affects the carrier collection in QNR, and thus it dominates the photo-generated current at large voltage-bias. This explains that the $J_{ph}(V)$ difference among these samples becomes larger as voltage-bias increases. Overall, the voltage-dependent photocurrent characteristics observed in this work are dominated by the carrier collection in QNR, which is affected by the parameter F_{Ga} and front sulfur-gradient.

B. Interpreting the empirical trend of FF

In literature, voltage-dependence on carrier collection has been reported to modify the ideal FF,⁵¹ and the modified FF is dependent on V_{oc} , A , and $\eta_c(V_{mpp})$.⁵²

$$FF \approx \eta_c(V_{mpp}) \left(1 - \frac{AV_T}{V_{oc}} \ln \left(\frac{V_{oc}}{AV_T} \right) \right), \quad (4)$$

where V_T is the thermal voltage that depends on the absolute temperature. The value of V_T is 26 mV at 300 K. The modified expression of FF shows positive dependence on both of the $\eta_c(V_{mpp})$ and V_{oc}/A factors. These two factors play critical roles in determining the empirical trend of FF.

In addition to the $\eta_c(V_{mpp})$ that has been discussed in Section V A, the empirical trend of V_{oc}/A is discussed here. In Fig. 6(c), the measured data show an increase of V_{oc}/A

from sample A to sample E. Furthermore, the influence of composition grading on V_{oc}/A is analyzed. In simulation, it reveals that an increased F_{Ga} can reduce SCR recombination rate and improve the V_{oc} , which is due to the enlarged bandgap in the front of the absorber. In addition, an increased F_{Ga} can decrease the CBM grading and result in the weaker back electric field. Under a forward bias, the weaker electric field reduces the blocking of electron injection into QNR. Consequently, the increased F_{Ga} leads to the reduced ratio of the integrated recombination rate in SCR over that in QNR, which results in a decreased ideal factor toward $A = 1$. By the same token, Orgis *et al.*⁵² found that a shift towards the dominance of SCR recombination can be created by a longer gradient length of back E_g grading. These findings point out that an increased back grading of CBM gives rise to an increased diode ideal factor and vice versa. Based on the above discussion, we can conclude that an increased F_{Ga} can lead to an improved V_{oc}/A by reducing SCR recombination and shifting the recombination center toward QNR. Similarly, an increased sulfur-gradient also can enlarge the surface E_g and improve the V_{oc}/A . Therefore, the evolution of bandgap profiling from sample A to sample E, which leads to the wider E_g and lower gradient of CBM, is beneficial for improving the V_{oc}/A .

The influence of composition grading on $\eta_c(V_{mpp})$ and V_{oc}/A has been studied in Sections V A and V B. By applying the above learning, the empirical trend of FF can therefore be interpreted. From sample A to sample D, the increased F_{Ga} significantly enlarges the bandgap in SCR and reduces the back grading of CBM. These changes lead to the reduced SCR recombination and the shift of recombination center toward QNR, which result in an increased V_{oc}/A (Fig. 6(c)). On the other hand, the reduced CBM grading also decreases the collection efficiency in QNR and results in a decreased $\eta_c(V_{mpp})$ (Fig. 10(b)). Because the V_{oc}/A improvement is over the $\eta_c(V_{mpp})$ degradation, an increased FF from sample A to sample D is resulted. For sample E, both the increased F_{Ga} and front sulfur-gradient can improve the V_{oc}/A . Nonetheless, the high F_{Ga} and sulfur-gradient form a detrimental bandgap grading to deteriorate the carrier collection in QNR, which causes severe $\eta_c(V_{mpp})$ drop by relative -16% (Fig. 10(b)). Because the $\eta_c(V_{mpp})$ drop prevails over the V_{oc}/A improvement, FF of sample E shows a considerable deterioration by relative -10% (Fig. 6(b)). Therefore, sample E shows much lower conversion efficiency even with the highest $V_{oc} \times J_{sc}$ (23.2 mW/cm^2). In conclusion, the trade-off between SCR recombination and QNR carrier collection, which can be affected by varied F_{Ga} and front sulfur-gradients, dominates the optimal FF and thus the conversion efficiency.

C. Co-optimization of the gallium and sulfur gradients

In this experiment, flatter gallium profiles can significantly improve the $V_{oc} \times J_{sc}$ but also may induce the synergistic effect with high sulfur-gradient to causes severe $\eta_c(V_{mpp})$ drop. Therefore, co-optimization of gallium and sulfur gradients in the absorber formation process plays an important role in producing high-efficiency CIGSeS solar

cell. For the quantitative investigation, device performances are simulated for varied F_{Ga} with two kinds of sulfur-gradients, S_U and S_L . In these devices, the elemental concentration is kept the same, and the gradient is varied. For the gallium profiles, F_{Ga} varied from 0% to 90% under a fixed $GGI_{avg} = 0.26$. For the sulfur profiles, there are two kinds of gradients, S_U and S_L . In Fig. 11(a), $\eta(S_U)$ and $\eta(S_L)$ represent conversion efficiency with S_U and S_L sulfur-gradients, respectively. η_{avg} is defined as the average efficiency of $\eta(S_U)$ and $\eta(S_L)$. $\Delta\eta$ is defined as the half of efficiency difference between $\eta(S_U)$ and $\eta(S_L)$. Conversion efficiency distribution due to the sulfur gradient variation can be described as $\eta_{avg} \pm \Delta\eta$.

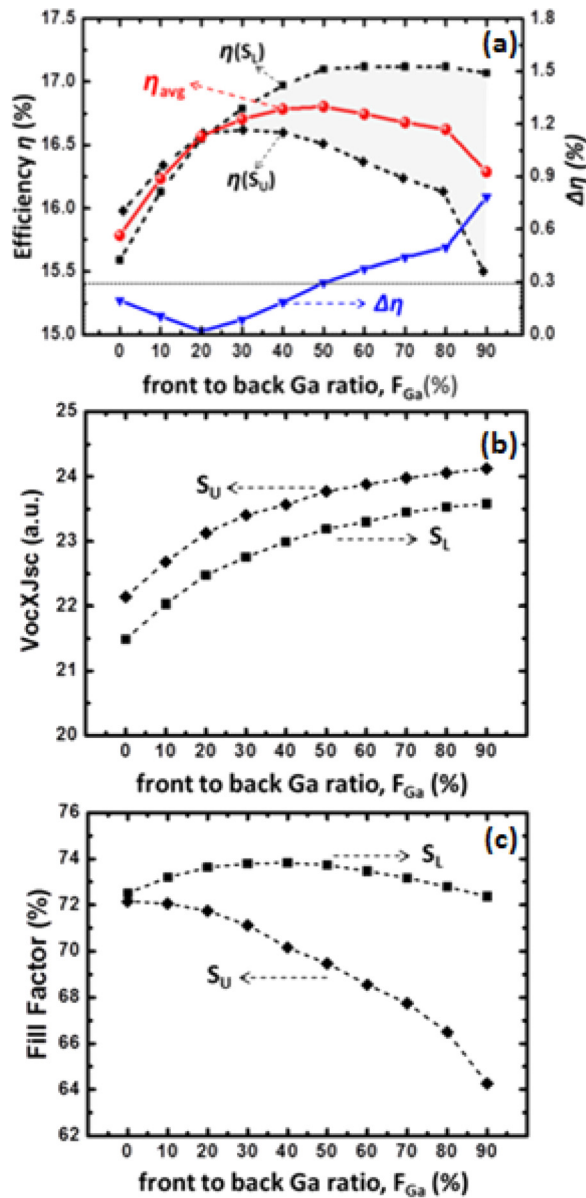


FIG. 11. Simulated device performance vs. F_{Ga} with S_U and S_L sulfur-gradients: (a) conversion efficiency η (b) $V_{oc} \times J_{sc}$, and (c) FF. The GGI_{avg} of simulated devices is kept at 0.26. $\eta(S_U)$ and $\eta(S_L)$ represent efficiency with S_U and S_L sulfur-gradients, respectively. η_{avg} is defined as the average efficiency of $\eta(S_U)$ and $\eta(S_L)$. $\Delta\eta$ is defined as the half of efficiency difference between $\eta(S_U)$ and $\eta(S_L)$. Efficiency distribution by the variation of sulfur-gradients can be described as $\eta_{avg} \pm \Delta\eta$.

As discussed above, the conversion efficiency is determined by the trend of FF. When $F_{Ga} < 20\%$, an increased sulfur-gradient can improve efficiency because the improvement of $V_{oc} \times J_{sc}$ is more significant than the FF loss (Figs. 11(b) and 11(c)). When $F_{Ga} > 20\%$, $\eta_c(V_{mpp})$ significantly decreases from S_L to S_U due to the synergistic effect of high F_{Ga} and sulfur-gradient (Fig. 10(b)). Consequently, higher sulfur-gradient causes severe FF drop and lower efficiency especially for high F_{Ga} (Figs. 11(a) and 11(c)). In Fig. 11(a), $F_{Ga} = 20\%$ shows zero performance difference to sulfur-gradient variation. For $F_{Ga} > 20\%$, the efficiency-difference $\Delta\eta$ by sulfur-gradient increases with increased F_{Ga} . Moreover, the optimal F_{Ga} also shifts toward a lower value as sulfur-gradient increases from S_L to S_U , which indicates that higher F_{Ga} needs lower sulfur-gradient and vice versa. To approach the maximum efficiency, the parameter F_{Ga} should be increased to $\geq 50\%$ under the controlled sulfur-gradient ($SS \leq 20\%$ and $D_p \geq 15\%$). This reveals that a higher efficiency can be achieved by flatter gallium profile with lower sulfur gradient, which corresponds to the experimental results in this work.

In selenized absorbers, gallium atoms tend to accumulate at the back-side, which needs higher sulfur-incorporation to improve the gallium-diffusion for the higher V_{oc} . However, sulfur-incorporation should be kept at low level to avoid “over-sulfuration” effect. In this work, varied gallium gradients of the selenized absorber are explored under low sulfur-incorporation. The experiment shows that the high F_{Ga} absorber can significantly improve the cell efficiency with proper sulfur-gradient. Through characterization and simulation, it can be understood that a low sulfur-gradient is preferred for reducing the carrier collection loss for high F_{Ga} absorbers. With the consideration of the Ga-S interaction, lower H_2S/N_2 concentration and longer sulfuration time should be considered in practice to reduce the sulfur-gradient, which can further enhance efficiency gain of high F_{Ga} absorbers.

D. The high-efficiency gallium profile with robustness against sulfur-gradient variation

Compound absorber typically shows a compositional variation as a function of depth, e.g., gradients of gallium and sulfur. The amount of Ga and S present in the CIGSeS absorber directly affects the bandgap and hence the device efficiency. In production, process variation is unavoidable, and the sensitivity of performance to variation should be factored in device optimization. For CIGSeS graded bandgap devices, even a small fluctuation on Ga or S can lead to an unacceptable bandgap profiling and thus the variability in conversion efficiency. In some cases, an optimal composition profiling for the highest conversion efficiency may not be practical for mass-production due to the high sensitivity to process variation. In our absorber formation technology, gallium-gradient controlled by N_2 annealing step shows lower variation as compared with the sulfur-gradient, which can be affected by H_2S gas reaction and Ga-S interaction effect. Therefore, in pursuit of high production efficiency,

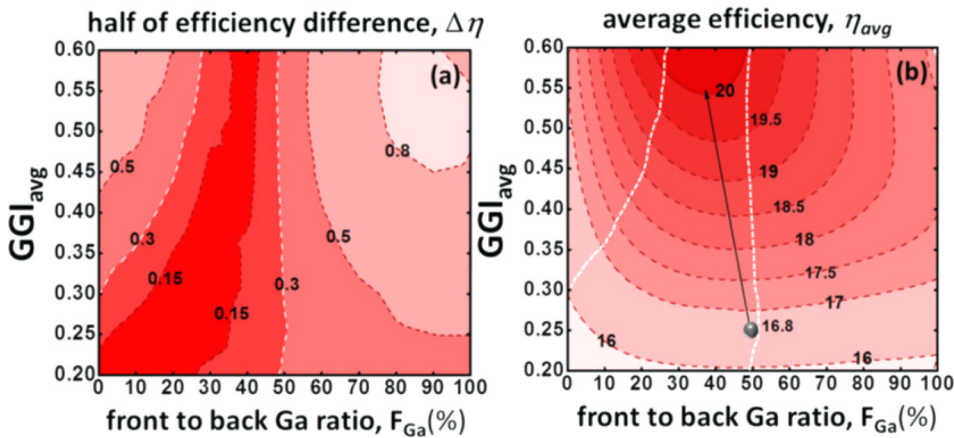


FIG. 12. Contour plots of $\Delta\eta$ and η_{avg} as a function of the parameter F_{Ga} and GGI_{avg} are shown in (a) and (b), respectively. High manufacturing yield window ($\Delta\eta < 0.3\%$) is plotted by the white dashed line. The arrow in (b) indicates a pathway toward $20 \pm 0.15\%$ conversion efficiency distribution from current optimal F_{Ga} at $GGI_{avg} = 0.26$, which has $16.8 \pm 0.3\%$ efficiency distribution.

optimal Ga-profile with sulfur-variation aware design should be considered.

Generally speaking, process variation of sulfur-gradient is expected even in a state-of-the-art CIGSeS production line. The possible variation is assumed to be bounded by the S_U and S_L sulfur-gradients. Here $\Delta\eta < 0.3\%$ is assumed as the requirement for high manufacturing yield. As shown in Fig. 11(a), $\Delta\eta$ by sulfur-gradient variation is larger than 0.3% for devices with $F_{Ga} > 50\%$, and it increases with increasing F_{Ga} due to the aforementioned synergistic effect. Thus, $F_{Ga} > 50\%$ is not a viable choice for manufacturing due to its high sensitivity to sulfur-gradient variation. As far as a high manufacturing yield is concerned, the Ga-profile with $F_{Ga} = 50\%$ is regarded as the optimal design which achieves the best efficiency distribution $16.8 \pm 0.3\%$ for the case of $GGI_{avg} = 0.26$.

The proposed TCAD modeling provides reliable predictions on the complicated interactions between composition gradients, device performances, and variability. Through the TCAD modeling, vast process parameters can be pre-screened to offer a path-finding function. Here varied Ga-profiles are explored to seek further efficiency improvement. Device performances are simulated for varied Ga-profiles with two kinds of sulfur profiles (S_L and S_U). The corresponding maps of $\Delta\eta$ and η_{avg} are shown in Figs. 12(a) and 12(b), respectively. Varied Ga-profiles are defined by F_{Ga} parameters and GGI_{avg} ratios. As shown in Fig. 12(a), $\Delta\eta$ is larger than 0.3% for $F_{Ga} > 50\%$. This is because $\Delta\eta_c$ (V_{mpp}) from the sulfur-gradient variation is more severe as F_{Ga} increases. For devices with overly steep Ga-profiles ($F_{Ga} < 10\%$), ΔV_{oc} is sensitive to the E_g variation in SCR. In GIGSeS material system (Fig. 9), the E_g dependence on $S/(Se + S)$ ratio is larger as $Ga/(Ga + In)$ ratio increases. The dependence leads to worse $\Delta\eta$ for overly steep Ga-profiles as GGI_{avg} ratio increases. As a result, the window of high manufacturing yield ($\Delta\eta < 0.3\%$) becomes narrowed as GGI_{avg} increases.

From the viewpoint of bandgap engineering, the increased $E_{g,min}$ with an optimal CBM grading allows us to improve the conversion efficiency along with robustness against sulfur-induced performance variability. For the absorber with overly flat ($F_{Ga} > 90\%$) and steep ($F_{Ga} < 10\%$) Ga-profiles, only an increase in GGI_{avg} does not bring appreciable improvement on η_{avg} but causes much worse $\Delta\eta$ as shown in Figs. 12(a) and 12(b). This reflects the uncontrollable efficiency variability on these approaches because of the

non-optimized Ga-profile to sulfur-variation. It is also seen from Figs. 11 and 12 that the modulation of F_{Ga} can lead to significant efficiency gain without losing performance stability. This point has been verified based on our experiments that an efficiency improvement from 15.4% (sample A) to 17.1% (sample D) for the case of $GGI_{avg} = 0.26$ is achieved by an increased F_{Ga} from 0% to 50%. Even more promisingly, a high-efficiency Ga-profile with robustness against sulfur-gradient variation is presented in Fig. 12(b). It indicates a pathway toward $20 \pm 0.15\%$ conversion efficiency distribution within high yield window. A further efficiency improvement of relative +19% can be achieved by an increased GGI_{avg} ratio to the range of 0.55–0.60 and decreased F_{Ga} to 40%. The modulation of both GGI_{avg} ratio and F_{Ga} leads to the improved bandgap profiling with greater tolerance to the sulfur-gradient variation. This also reveals that the optimal gallium profiling can contribute considerable manufacturing efficiency enhancement of a state-of-the-art CIGSeS production line. Moreover, it should be noted that performance sensitivity to F_{Ga} variation becomes higher with an increased GGI_{avg} ratio (Fig. 12(b)), which indicates that the process controllability in gallium-gradient is the most critical factor as approaching the higher efficiency.

Based on the simulated results, a V_{oc} saturation problem is observed if GGI_{avg} ratio is larger than 0.6 due to the increased recombination at the absorber/buffer interface, which is caused by near-zero or negative conduction band offset (cliff-like junction) at wide bandgaps. Such behavior has been observed experimentally in wide bandgap $Cu(In,Ga)Se_2$ devices and related discussion can be found in Refs. 53–56. From the viewpoint of band alignment, sulfur-incorporation in the surface region of $Cu(In,Ga)(Se,S)_2$ devices can reduce V_{oc} saturation behavior at wider bandgaps because a part of bandgap widening is in the valence band.⁵³ This feature allows a wide bandgap $Cu(In,Ga)(Se,S)_2$ device to have higher efficiency headroom than the reported $Cu(In,Ga)Se_2$ devices.^{53–56} Besides, the influence of high gallium content in CIGSeS crystalline quality is unknown and needs further studies when we are approaching the high efficient Ga-profile.

VI. SUMMARY AND CONCLUSION

In this work, the co-optimization of gallium and sulfur gradients in ternary $Cu(In,Ga)(Se,S)_2$ thin film solar cell

and their impacts on performance and variability are investigated experimentally and theoretically. An absorber formation method to modulate gallium profile under low sulfur-incorporation is disclosed. Flatter gallium profiles are demonstrated to provide a significant efficiency gain with improved $V_{oc} \times J_{sc}$, which is attributed to better matching between the bandgap profiling and the solar spectrum. An optimal Ga-profile achieving 17.1% conversion efficiency ($V_{oc} = 668$ mV, $J_{sc} = 34.9$ mA/cm², and $FF = 73.6\%$) on a 30 cm \times 30 cm sub-module **without anti-reflection coating (ARC)** is presented. Detailed film analysis and numerical simulation are performed to disclose the underlying physics of empirical observations.

Voltage-dependence on carrier collection for varied front-to-back Ga ratio (F_{Ga}) and front sulfur-gradients is investigated through photocurrent characteristics measurement and device simulation. It is concluded that the conduction-band grading by an increased F_{Ga} and front sulfur gradient is detrimental to the collection of photo-generated electrons. With an increased F_{Ga} , insufficient back grading of CBM reduces carrier collection efficiency, especially in QNR. The increased front sulfur-gradient also deteriorates QNR carrier collection due to the increased front energy barrier across the absorber/buffer interface. A synergistic effect of these two factors is found to incur severe $\eta_c(V_{mpp})$ loss, which can deteriorate FF and therefore the conversion efficiency.

Influences of varied F_{Ga} and front sulfur-gradients on carrier recombination are also investigated for CIGSeS solar cell with graded bandgap structure. Experiments reveal that the recombination current in these devices is dominated by the recombination paths in SCR. The bandgap and band grading in SCR can be tuned by varied F_{Ga} and front sulfur-gradient, and consequently diode quality is affected. An increased F_{Ga} gives rise to a decreased recombination rate in SCR by wider E_g and a shift of recombination path toward QNR by decreased conduction-band grading. The combination of such effects increases V_{oc} and decreases ideal factor toward $A = 1$. The same effects on V_{oc} and A can be resulted from the aid of front sulfur-gradient because SCR recombination can be further suppressed.

A clear physical picture is therefore presented to understand the complex trade-off between SCR recombination and QNR carrier collection, which is affected by the gallium and sulfur gradients. Our interpretation can successfully address the empirical observations that cannot be explained by standard solar circuit model, which includes the puzzling trend of FF, distortion of illuminated J-V curves, and voltage-dependent photocurrent characteristics. Additionally, the co-optimization of gallium and sulfur-gradient is further investigated. The experimental and simulation results show that a flatter gallium profile with lower sulfur gradient is a key factor in achieving high-efficiency CIGSeS solar cell. The gallium-flattening provides a different approach as compared with the case of Ga-accumulation by SAS method. For further process tuning of this work, lower H_2S/N_2 concentration and longer sulfuration time should be considered to reduce sulfur-gradient, which can further reduce carrier collection loss for efficiency improvement.

Performance variability induced by sulfur-gradient variation is also studied through compact device modeling, which shows reliable predictions on the complex interactions between composition gradients, performances, and variability. A gallium profiling guideline for suppressing sulfur-induced variability is proposed. It is suggested that gallium profiles with $F_{Ga} > 50\%$ are not suitable for mass-production because of their high-performance sensitivity to sulfur-gradient variation. This is because $\Delta\eta_c(V_{mpp})$ from sulfur variation is worse as F_{Ga} increases. Additionally, sulfur-induced efficiency variability becomes worse as the averaged GGI ratio (GGI_{avg}) increases, especially for the overly flat ($F_{Ga} > 90\%$) and overly steep ($F_{Ga} < 10\%$) cases. The presented results indicate that sulfur-gradient variation is critical for the conversion efficiency distribution of a state-of-the-art CIGSeS production line. The headroom for further efficiency improvement is studied through exploring varied gallium profiling under different sulfur-gradients. Finally, $20 \pm 0.15\%$ conversion efficiency distribution is reached by an optimal gallium profile with an averaged GGI ratio (GGI_{avg}) of 0.55–0.60 and front-to-back Ga ratio (F_{Ga}) of 40%. This optimal gallium profile also leads to greater tolerance to the sulfur-gradient variation of surface S/(Se + S) = 19%–30% and normalized penetration depth = 11%–18%.

¹P. Jackson, D. Hariskos, R. Wuerz, O. Kiowski, A. Bauer, T. M. Friedlmeier, and M. Powalla, *Phys. Status Solidi RRL* **9**, 28–31 (2015).

²D. Herrmann *et al.*, “CIGS module manufacturing with high deposition rates and efficiencies,” paper presented at 40th IEEE, PVSC, Denver, CO, USA, 8–13 June 2014.

³A. Goetzberger, C. Hebling, and H.-W. Schock, *Mater. Sci. Eng., R* **40**, 1–46 (2003).

⁴S. Niki, M. Contreras, I. Repins, M. Powalla, K. Kushiya, S. Ishizuka, and K. Masubara, *Prog. Photovoltaics* **18**, 453–566 (2010).

⁵V. Alberts, J. Titus, and R. W. Birkmire, *Thin Solid Films* **451–452**, 207–211 (2004).

⁶K. Kushiya, “CIS-based thin-film PV technology in solar frontier K.K.,” *Sol. Energy Mater. Sol. Cells* **122**, 309–313 (2014).

⁷S. Yang, K. M. Lin, W. C. Lee, C. C. Lin, and L. Chu, “Achievement of 15.1% total area efficiency on 1.09 m² monolithic CIGSeS modules in TSMC solar production line,” in 39th IEEE Photovoltaic Specialists Conference (2013).

⁸A. Chirilă, P. Reinhard, F. Pianezzi, P. Bloesch, A. R. Uhl, C. Fella, L. Kranz, D. Keller, C. Gretener, H. Hagendorfer, D. Jaeger, R. Erni, S. Nishiwaki, S. Buecheler, and A. N. Tiwari, *Nat. Mater.* **12**, 1107 (2013).

⁹K. Ramanathan, M. A. Contreras, C. L. Perkins, S. Asher, F. S. Hasoon, J. Keane, D. Young, M. Romero, W. Metzger, R. Noufi, J. S. Ward, and A. Duda, *Prog. Photovoltaics* **11**, 225–230 (2003).

¹⁰I. Repins, M. A. Contreras, B. Egaas, C. DeHart, J. Scharf, C. L. Perkins, B. To, and R. Noufi, *Prog. Photovoltaics* **16**, 235–239 (2008).

¹¹M. Powalla, P. Jackson, W. Witte, D. Hariskos, S. Paetel, C. Tschamber, and W. Wischmann, *Sol. Energy Mater. Sol. Cells* **119**, 51–58 (2013).

¹²S.-H. Wei and A. Zunger, *J. Appl. Phys.* **78**, 3846 (1995).

¹³S. Chen, X. G. Gong, and S.-H. Wei, *Phys. Rev. B* **75**, 205209–1 (2007).

¹⁴M. Marudachalam, H. Hichri, R. Klenk, R. W. Birkmire, and W. N. Shafarman, *Appl. Phys. Lett.* **67**, 3978–3980 (1995).

¹⁵R. Kamada, W. N. Shafarman, and R. W. Birkmire, *Sol. Energy Mater. Sol. Cells* **94**, 451–456 (2010).

¹⁶R. Caballero, C. Guillen, M. T. Gutierrez, and C. A. Kaufmann, *Prog. Photovoltaics* **14**, 145–153 (2006).

¹⁷G. M. Hanket, W. N. Shafarman, B. E. McCandless, and R. W. Birkmire, *J. Appl. Phys.* **102**, 074922-1–074922-10 (2007).

¹⁸Y. Goushi, H. Hakuma, K. Tabuchi, S. Kijima, and K. Kushiya, *Sol. Energy Mater. Sol. Cells* **93**(8), 1318–1320 (2009).

¹⁹TSMC Solar Commercial-size Modules (1.09m²) Set CIGS 15.7% Efficiency Record, TSMC Solar 2013 Press Release, June 18.

- ²⁰TSMC Solar Commercial-size Modules (1.09m²) Set CIGS 16.5% Efficiency Record, TSMC Solar 2015 Press Release, April 28.
- ²¹O. Lundberg, J. Lu, A. Rockett, M. Edoff, and L. Stolt, *J. Phys. Chem. Solids* **64**(9–10), 1499 (2003).
- ²²O. Knacke, O. Kubaschewski, and K. Hesselmann, *Thermo-Chemical Properties of Inorganic Substances*, 2nd ed. (Springer-Verlag, Heidelberg, 1991).
- ²³W. K. Metzger, I. L. Repins, M. Romero, P. Dippo, M. Contreras, R. Noufi, and D. Levi, *Thin Solid Films* **517**, 2360 (2009).
- ²⁴S. S. Hegedus and W. N. Shafarman, *Prog. Photovoltaics* **12**, 164–169 (2004).
- ²⁵P. Würfel, *Physics of Solar Cells: From Principles to New Concepts* (Wiley-VCH, Weinheim, 2005), p. 138.
- ²⁶F. A. Lindholm, J. G. Fossum, and E. L. Burgess, *IEEE Trans. Electron Devices* **26**, 165 (1979); in *12th IEEE Photovoltaic Specialists Conference* (1976), p. 33.
- ²⁷K. Mitchell, A. Fahrenbruch, and R. Bube, *J. Appl. Phys.* **48**, 4365 (1977).
- ²⁸A. Rothwarf, J. Phillips, and N. Wyeth, in *Proceedings of 13th IEEE Photovoltaic Specialists Conference* (1978), p. 399.
- ²⁹R. A. Crandall, *J. Appl. Phys.* **53**, 3350 (1982).
- ³⁰J. Phillips, J. Titus, and D. Hoffman, in *Proceedings of 26th IEEE Photovoltaic Specialists Conference* (1997), p. 463.
- ³¹K. Hecht, *Z. Phys.* **77**, 235 (1932).
- ³²T. Markvart, *IEEE Trans. Electron Devices* **44**, 1182 (1997).
- ³³R. S. Crandall, *J. Appl. Phys.* **54**, 7176 (1983).
- ³⁴M. Wolf, *Proc. IEEE* **51**, 674 (1963).
- ³⁵D. J. Friedman, A. J. Ptak, S. R. Kurtz, and J. F. Geisz, in *Conference Record of the 31th IEEE Photovoltaic Specialists Conference* (2005), p. 691.
- ³⁶R. S. Crandall, *J. Appl. Phys.* **55**, 4418 (1984).
- ³⁷E. A. Schiff, *Sol. Energy Mater. Sol. Cells* **78**, 567 (2003).
- ³⁸C. Donolato, *Appl. Phys. Lett.* **46**, 270 (1985).
- ³⁹K. Misiakos and F. A. Lindholm, *J. Appl. Phys.* **58**, 4743 (1985).
- ⁴⁰S. Hegedus *et al.*, *Prog. Photovoltaics* **15**, 587 (2007).
- ⁴¹X. Liu and J. Sites, *J. Appl. Phys.* **75**, 577 (1994).
- ⁴²K. Misiakos and F. Lindholm, *J. Appl. Phys.* **64**, 383 (1988).
- ⁴³T. H. Glisson, J. R. Hauser, M. A. Littlejohn, and C. J. Williams, *J. Electron. Mater.* **7**, 1 (1978).
- ⁴⁴S. Adachi, *J. Appl. Phys.* **61**(10), 4869–4876 (1987).
- ⁴⁵K. Kim *et al.*, *Prog. Photovoltaics* **23**, 765–772 (2015).
- ⁴⁶D. S. Albin, J. R. Tuttle, G. D. Mooney, J. J. Carapella, A. Duda, A. Mason, and R. Noufi, in *The Conference Record of the 21st IEEE Photovoltaic Specialists Conference* (IEEE, New York, 1990), p. 562.
- ⁴⁷P. D. Paulson, R. W. Birkmire, and W. N. Shafarman, *J. Appl. Phys.* **94**, 879 (2003).
- ⁴⁸M. I. Alonso, K. Wakita, J. Pascual, M. Garriga, and N. Yamamoto, *Phys. Rev. B* **63**, 075203 (2001).
- ⁴⁹J. W. Lee, J. D. Cohen, and W. N. Shafarman, *Thin Solid Films* **480–481**, 336 (2005).
- ⁵⁰M. Gloeckler, Ph.D. thesis, Colorado State University, 2005.
- ⁵¹A. de Vos, *Sol. Cells* **8**, 283 (1983).
- ⁵²Th. Orgis, M. Malberg, and R. Scheer, *J. Appl. Phys.* **114**, 214506 (2013).
- ⁵³M. Gloeckler and J. R. Sites, “Efficiency limitations for wide-band-gap chalcopyrite solar cells,” *Thin Solid Films* **480–481**, 241–245 (2005).
- ⁵⁴X. Liu and J. R. Sites, *AIP Conf. Proc.* **353**, 444 (1996).
- ⁵⁵R. Scheer, *Trends Vac. Sci. Technol.* **2**, 77 (1997).
- ⁵⁶T. Minemoto, T. Matsui, H. Takakura, Y. Hamakawa, T. Negami, Y. Hashimoto, T. Uenoyama, and M. Kitagawa, *Sol. Energy Mater. Sol. Cells* **67**, 83 (2001).